

X-ray spectral components of the blazar and binary black hole candidate OJ 287 (2005–2020)

S. Komossa,^{1*} D. Grupe,² M.L. Parker,^{3,4} J.L. Gómez,⁵ M.J. Valtonen,^{6,7} M.A. Nowak,⁸ S.G. Jorstad,^{9,10} D. Haggard,^{11,12} S. Chandra,¹³ S. Ciprini,^{14,15} L. Dey,¹⁶ A. Gopakumar,¹⁶ K. Hada,¹⁷ S. Markoff,¹⁸ J. Neilsen¹⁹

¹Max-Planck-Institut für Radioastronomie, Auf dem Hügel 69, 53121 Bonn, Germany

²Department of Physics, Earth Science, and Space System Engineering, Morehead State University, 235 Martindale Dr, Morehead, KY 40351, USA

³European Space Agency (ESA), European Space Astronomy Centre (ESAC), E-28691 Villanueva de la Canada, Madrid, Spain

⁴Institute of Astronomy, University of Cambridge, Madingley Road, Cambridge CB3 0HA, UK

⁵Instituto de Astrofísica de Andalucía-CSIC, Glorieta de la Astronomía s/n, E-18008 Granada, Spain,

⁶Finnish Centre for Astronomy with ESO, University of Turku, FI-20014, Turku, Finland

⁷Department of Physics and Astronomy, University of Turku, FI-20014, Turku, Finland

⁸Department of Physics, Washington University in St. Louis, One Brookings Dr., St. Louis, MO 63130-4899, USA

⁹Institute for Astrophysical Research, Boston University, 725 Commonwealth Ave, Boston, MA 02215, USA

¹⁰Sobolev Astronomical Institute, St. Petersburg State University, St. Petersburg, Russia

¹¹Department of Physics, McGill University, 3600 rue University, Montréal, QC H3A 2T8, Canada

¹²McGill Space Institute, McGill University, 3550 rue University, Montréal, QC H3A 2A7, Canada

¹³Centre for Space Research, North-West University, Potchefstroom 2520, South Africa

¹⁴Istituto Nazionale di Fisica Nucleare (INFN) Sezione di Roma Tor Vergata, Via della Ricerca Scientifica 1, 00133, Roma, Italy

¹⁵ASI Space Science Data Center (SSDC), Via del Politecnico, 00133, Roma, Italy

¹⁶Department of Astronomy and Astrophysics, Tata Institute of Fundamental Research, Mumbai 400005, India

¹⁷Department of Astronomical Science, The Graduate University for Advanced Studies (SOKENDAI), 2-21-1 Osawa, Mitaka, Tokyo 181-8588, Japan

¹⁸API–Anton Pannekoek Institute for Astronomy, University of Amsterdam, Science Park 904, 1098 XH Amsterdam, The Netherlands

¹⁹Villanova University, 800 E. Lancaster Avenue, Villanova, PA 19085, USA

Accepted 2021 April 23. Received 2021 April 16; in original form 2021 January 13

ABSTRACT

We present a comprehensive analysis of all XMM-Newton spectra of OJ 287 spanning 15 years of X-ray spectroscopy of this bright blazar. We also report the latest results from our dedicated Swift UVOT and XRT monitoring of OJ 287 which started in 2015, along with all earlier public Swift data since 2005. During this time interval, OJ 287 was caught in extreme minima and outburst states. Its X-ray spectrum is highly variable and encompasses all states seen in blazars from very flat to exceptionally steep. The spectrum can be decomposed into three spectral components: Inverse Compton (IC) emission dominant at low-states, super-soft synchrotron emission which becomes increasingly dominant as OJ 287 brightens, and an intermediately-soft ($\Gamma_x = 2.2$) additional component seen at outburst. This last component extends beyond 10 keV and plausibly represents either a second synchrotron/IC component and/or a temporary disk corona of the primary supermassive black hole (SMBH). Our 2018 XMM-Newton observation, quasi-simultaneous with the Event Horizon Telescope observation of OJ 287, is well described by a two-component model with a hard IC component of $\Gamma_x = 1.5$ and a soft synchrotron component. Low-state spectra limit any long-lived accretion disk/corona contribution in X-rays to a very low value of $L_x/L_{\text{Edd}} < 5.6 \times 10^{-4}$ (for $M_{\text{BH,primary}} = 1.8 \times 10^{10} M_\odot$). Some implications for the binary SMBH model of OJ 287 are discussed.

Key words: galaxies: active – galaxies: jets – galaxies: nuclei – quasars: individual (OJ 287) – quasars: supermassive black holes – X-rays: galaxies

1 INTRODUCTION

The blazar OJ 287 is perhaps the first identified multi-messenger source among extragalactic supermassive black holes. As one of the

* E-mail: astrokomossa@gmx.de (SK)

best candidates for hosting a compact supermassive binary black hole (SMBBH) and known as a bright blazar, it has been intensely observed across the *electromagnetic* regime. Further, modelling of its optical/IR light curve has revealed evidence for mild orbital shrinkage due to the emission of *gravitational waves* (GWs; Valtonen et al. 2008; Laine et al. 2020). While not yet directly detected, GWs from this system may become measurable with the next generation of pulsar-timing arrays (PTAs) based on planned radio-telescope facilities (Yardley et al. 2010).

Coalescing SMBBHs which form in galaxy mergers are the loudest sources of low-frequency GWs in the universe (Centrella et al. 2010; Kelley et al. 2019). An intense electromagnetic search for wide and close binaries in all stages of their evolution is therefore ongoing (review by Komossa & Zensus 2016). While wide pairs can be identified by spatially-resolved imaging spectroscopy, indirect methods are required for detecting the most compact, evolved systems. These latter systems are well beyond the “final parsec” in their evolution (Begelman et al. 1980; Colpi 2014) and in a regime where GW emission contributes to, or dominates, their orbital shrinkage. Semi-periodicity in light curves has become a major tool for selecting these small-separation SMBBH candidates (e.g., Graham et al. 2015).

OJ 287 is a nearby, bright BL Lac object at redshift $z = 0.306$ and among the best candidates to date for hosting a compact SMBBH (Sillanpää et al. 1988; Valtonen et al. 2016). Its unique optical light curve spans more than a century and dates back to the late 19th century. It shows optical double-peaks every ~ 12 years, which have been interpreted as arising from the orbital motion of a pair of SMBHs, with an orbital period on that order (~ 9 yrs in the system’s rest frame).

While different variants of binary scenarios of OJ 287 were considered in the past (e.g., Lehto & Valtonen 1996; Katz 1997; Valtaoja et al. 2000; Villata et al. 1998; Liu & Wu 2002; Qian 2015; Britzen et al. 2018; Dey et al. 2018), the best explored and most successful model explains the double peaks as the times when the secondary SMBH impacts the disk around the primary twice during its ~ 12 yr orbit (“impact flares” hereafter). The most recent orbital two-body modelling is based on 4.5 order post-Newtonian dynamics and successfully reproduces the overall long-term light curve of OJ 287 until 2019 (Valtonen et al. 2016; Dey et al. 2018; Laine et al. 2020, and references therein), with impact flares observed most recently in 2015 and 2019. The model requires a compact binary with a semi-major axis of 9300 AU with a massive primary SMBH of $1.8 \times 10^{10} M_{\odot}$, and a secondary of $1.5 \times 10^8 M_{\odot}$. Because of the strong general-relativistic precession of the secondary’s orbit, $\Delta\Phi=38$ deg/orbit, the impact flares are not always separated by 12 yrs, instead their separation varies strongly with time in a predictable manner. In addition to the impact flares, the model predicts “after-flares” when the impact disturbance reaches the inner accretion disk (Sundelius et al. 1997; Valtonen et al. 2009; Pihajoki et al. 2013), identified most recently with the bright X-ray–UV–optical outburst in 2020 (Komossa et al. 2020a).

First detected as a radio source during the Vermilion River Observatory Sky Survey (Dickel et al. 1967) and the Ohio Sky Survey (Kraus 1977), OJ 287 has been studied extensively in the radio regime. Its relativistic jet is pointing at us with an average viewing angle of ~ 2 degrees (Jorstad et al. 2005; Agudo et al. 2012) and shows remarkable short-timescale variability interpreted as a turbulent injection process and/or a clumpy accretion disk structure (Agudo et al. 2012) or as a binary-induced wobble (Valtonen & Pihajoki 2013; Dey et al. 2021). The inner jet is the source of highly variable γ -rays (e.g., Hodgson et al. 2017; Agudo et al. 2011)

and displays strong and variable radio polarization (e.g., Aller et al. 2014; Myserlis et al. 2018; Cohen et al. 2018). Though only faintly detected in the very-high energy (VHE) band (>100 GeV; Mukherjee et al. 2017; O’Brien 2017), OJ 287 is a well-known X-ray emitter and has been detected with most major X-ray observatories, including Einstein (Madejski & Schwartz 1988), EXOSAT (Sambruna et al. 1994), ROSAT (Comastri et al. 1995), BeppoSAX (Massaro et al. 2003), ASCA (Idesawa et al. 1997), the Neil Gehrels Swift observatory (Swift hereafter; Massaro et al. 2008), Suzaku (Seta et al. 2009), XMM-Newton (Ciprini et al. 2007) and most recently with NuSTAR (Komossa et al. 2020a). These observations established OJ 287 as a bright and variable X-ray source, and allowed single-component X-ray spectral fits. Its (0.5–10) keV X-ray spectrum was interpreted as a mix of synchrotron and inverse Compton (IC) emission, with the former more variable (Urry et al. 1996). OJ 287 is found most of the time in a rather flat spectral state with a photon index $\Gamma_x \approx 1.5 - 1.9$, though Γ_x is as steep as 2.6 during one ROSAT observation (Urry et al. 1996) in the band (0.1–2.4) keV. Its steepest state, with an equivalent $\Gamma_x = 2.8$, (better fit with a logarithmic parabolic model) was detected with XMM-Newton in the band (0.3–10) keV, which caught the source right at the peak of one of the brightest X-ray outbursts measured so far (Komossa et al. 2020a). Imaging with the Chandra X-ray observatory has revealed a long, curved X-ray jet consisting of multiple knots and extending out to $20''$ or a de-projected scale of > 1 Mpc, and bright central emission (Marscher & Jorstad 2011).

The optical spectrum of OJ 287 is often featureless, even though some narrow emission lines and broad $H\alpha$ are occasionally detected in low-states and have been used to determine the redshift of OJ 287 (Sitko & Junkkarinen 1985; Stickel et al. 1989). $H\alpha$ had decreased by a factor of 10 when re-observed in 2005–2008 (Nilsson et al. 2010). The overall faintness of the broad Balmer lines is the basis for the classification of OJ 287 as a BL Lac object.

We are carrying out a dedicated multi-year, multi-frequency monitoring program of OJ 287 with Swift and in the radio regime. This MOMO program (for Multi-wavelength Observations and Modelling of OJ 287) includes a search for outbursts and explores and tests facets of the binary SMBH model. Previous results from this program were presented by Komossa et al. (2017, flux and spectral evolution during the 2016/17 outburst), by Myserlis et al. (2018, radio monitoring), and by Komossa et al. (2020a, 2020 outburst and long-term lightcurve; “paper I” hereafter). Exceptional outbursts or low-states of OJ 287 detected by Swift were initially reported within days in a sequence of *Astronomer’s Telegrams* (e.g., Komossa et al. 2015; Grupe et al. 2016, 2017; Komossa et al. 2018, 2020b,c,d) to inform the community and encourage observations in bands not densely covered by our campaigns, like the near infrared (Kushwaha et al. 2018). Independent of the binary’s presence, OJ 287 is a nearby bright blazar, and dense multi-frequency monitoring and high-resolution X-ray spectroscopy are powerful diagnostics of jet and accretion physics in blazars. Results of the MOMO program continue to be presented in a sequence of publications. Here, in the fourth study, we present XMM-Newton and Swift X-ray spectroscopy of OJ 287, spanning a time interval of 1.5 decades and covering the most extreme X-ray flux and spectral states so far observed.

This paper is structured as follows. In Sect. 2 we discuss the long-term Swift data with focus on the X-ray spectral variability properties and a softer-when-brighter variability pattern. A spectral and temporal analysis of all XMM-Newton data of OJ 287 is provided in Sect. 3. In Sect. 4, implications for emission models and the binary SMBH nature of OJ 287 are discussed. A summary and con-

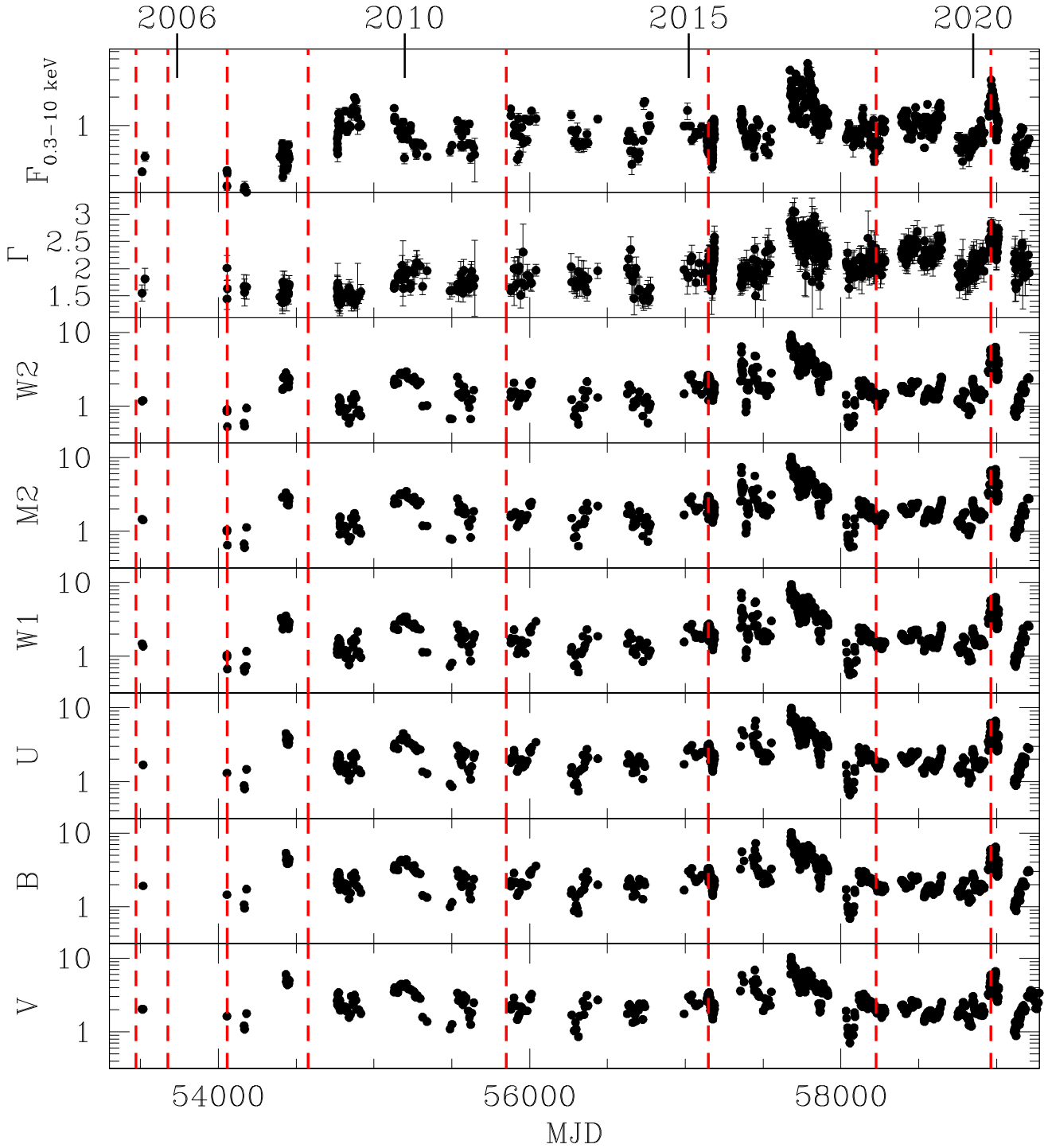


Figure 1. Swift XRT and UVOT light curves of OJ 287 between 2005 and December 2020 since the beginning of Swift monitoring. Epochs of XMM-Newton observations are marked by vertical, dashed, red lines. The observed X-ray flux (0.3–10 keV, corrected for Galactic absorption) and the optical-UV fluxes (corrected for extinction) are given in units of 10^{-11} $\text{erg s}^{-1} \text{cm}^{-2}$. Γ_x is the X-ray power-law photon index. January 1st of each of the years 2006, 2010, 2015 and 2020 is marked on the upper horizontal axis. Error bars are always reported, but are often smaller than the symbol size.

clusions are provided in Sect. 5. A cosmology (Wright 2006) with $H_0=70 \text{ km s}^{-1} \text{Mpc}^{-1}$, $\Omega_M=0.3$ and $\Omega_\Lambda=0.7$ is used throughout this paper.

2 SWIFT DATA ANALYSIS AND SPECTRAL FITS

2.1 Swift XRT

We have monitored OJ 287 with Swift (Gehrels et al. 2004) since December 2015 (Komossa et al. 2017, 2020a, our Fig. 1). A ca-

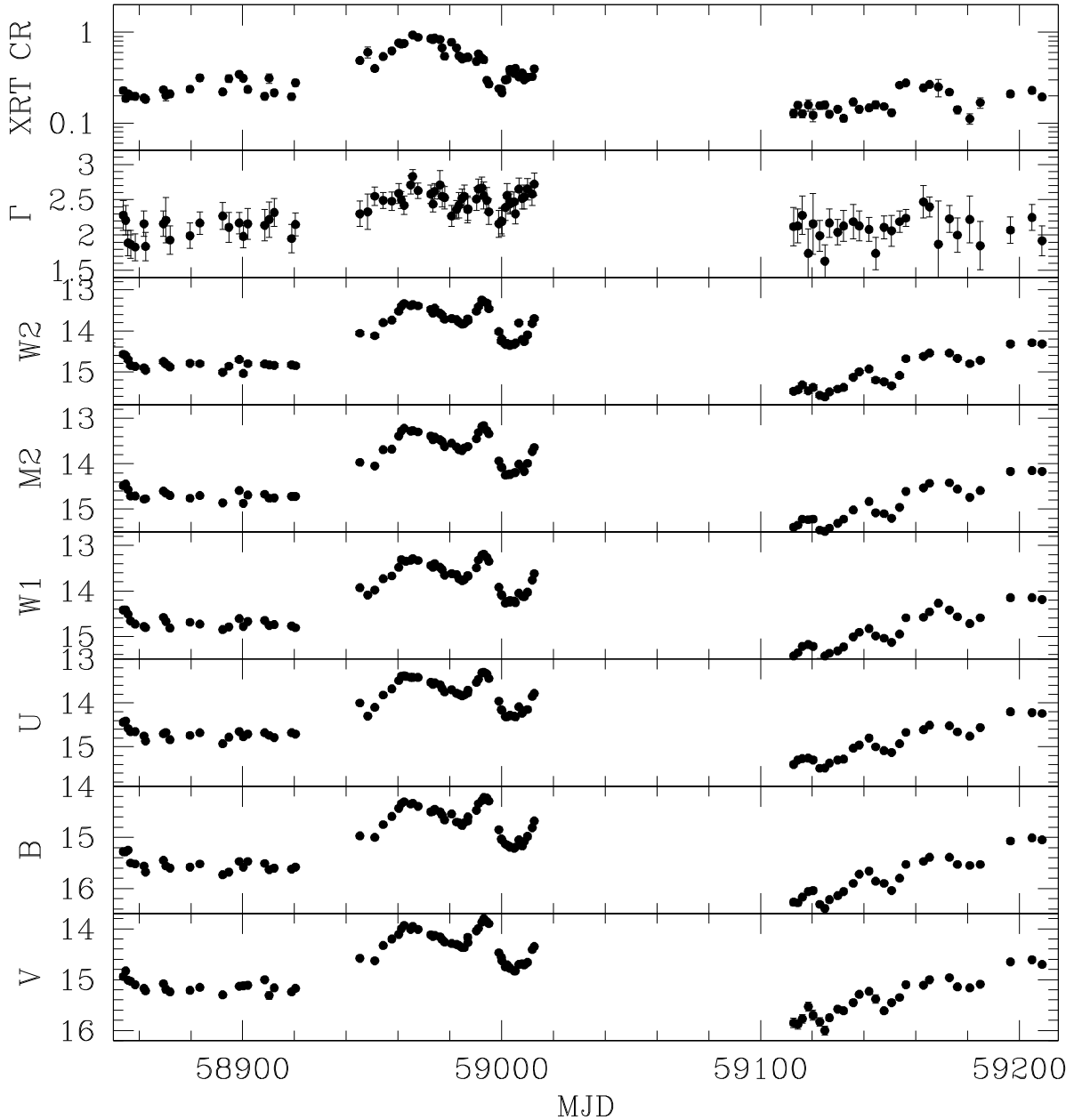


Figure 2. 2020 Swift light curve (XRT countrate in cts s^{-1} , photon index Γ_x , and observed UVOT magnitudes in the VEGA system) of OJ 287 obtained in the course of the MOMO program, including the April–June 2020 outburst (Komossa et al. 2020a) and the newly detected deep September 2020 optical-UV low-state when OJ 287 emerged from Swift Sun constraint. Error bars are always reported, but are often smaller than the symbol size.

Table 1. Log of observations of our new 2020 Swift data since September 2020. The third column gives the dates of the observations and the fourth column reports the duration of each single observation in ks.

instrument	band/filter	date	Δt (ks)
XRT	0.3–10 keV	Sept.–Dec. 2020	0.5–2
UVOT	W2	Sept.–Dec. 2020	0.12–0.6
	M2		0.09–0.5
	W1		0.06–0.3
	U		0.03–0.16
	B		0.03–0.16
	V		0.03–0.16

dence of ~ 3 –7 days was employed and increased to 1–2 days at some epochs of outbursts or low-states. We also enhanced the already dense monitoring cadence of OJ 287 during the epochs of the Event Horizon Telescope (EHT hereafter; Event Horizon Telescope Collaboration et al. 2019) coverage in April 2017 and 2018.

Our monitoring was resumed in September 2020 (Tab. 1, Fig. 2; OBS-ID 35905-89...35905-117), when OJ 287 became visible again after its Swift Sun constraint. We found that the bright April–May 2020 outburst was over, and OJ 287 was caught in a deep low-state at all wavebands. The light curve is reported here for the first time. The community was informed about the low-state in an *Astronomer’s Telegram* (Komossa et al. 2020d). During these new 2020 observations, the Swift X-ray telescope (XRT; Burrows et

al. 2005) was operating in *photon counting* (PC) mode (Hill et al. 2004). Exposure times range between 0.5–2 ks.

To inspect the long-term light curve, and obtain the X-ray and UVOT flux evolution before and after the epochs of the early XMM-Newton observations (Sect. 3) as well, we have also created the Swift UVOT and XRT light curve of OJ 287 between 2005 and 2015 based on all public archival data. Further, we have added all of the few data after 2015 which were not part of our own dedicated monitoring program. Before late 2015 the Swift coverage of OJ 287 was overall more sparse, with the exception of a dense monitoring campaign in mid-2015 (PI: R. Edelson). Many of the remaining pre-2015 data were obtained in the course of a blazar monitoring program (Massaro et al. 2008; Stroh & Falcone 2013; Williamson et al. 2014; Siejkowski & Wierzholska 2017) and a dedicated early study of OJ 287 (Valtonen et al. 2016). The majority of these XRT data were taken in PC mode, while data above ~ 1 cts s^{-1} were obtained in *windowed timing* (WT) mode (Hill et al. 2004).

X-ray countrates were determined using the XRT product tool at the Swift data centre in Leicester (Evans et al. 2007). To carry out the X-ray spectral analysis, source photons were extracted within a circle of $47''$ radius. OJ 287 is off-axis in most observations, as is typical for Swift monitoring programs. The source extraction size does include the $20''$ X-ray jet detected with the Chandra observatory. However, the integrated Chandra ACIS-S jet emission of ~ 0.03 cts s^{-1} with an average $\Gamma_x = 1.61$ (Marscher & Jorstad 2011) only amounts to a Swift XRT countrate of 0.009 cts s^{-1} , negligibly contributing to the integrated emission even in X-ray low-states. Background photons were collected in a nearby circular region of radius $236''$. X-ray spectra in the band (0.3–10) keV were then generated and the software package *xSPEC* (version 12.10.1f; Arnaud 1996) was used for analysis.

Swift data above a countrate of ~ 0.7 cts s^{-1} are affected by pile-up. To correct for it, the standard procedure was followed of first creating a region file where the inner circular area of the PSF was excluded from the analysis. The loss in counts is then corrected by creating a new ancillary response file based on this annular region that is used in *xSPEC* to correct the flux measurement.

Spectra were fit with single power laws of photon index Γ_x adding Galactic absorption (Wilms et al. 2000) along our line-of-sight with a Hydrogen column density $N_{H, Gal} = 2.49 \times 10^{20}$ cm^{-2} (Kalberla et al. 2005), and using the W-statistics of *xSPEC* on the unbinned data. (W-statistics are used when countrates are low so that data follow Poisson statistics, and when not only a source but also a background spectrum is available.)

OJ 287 displays a strong softer-when-brighter variability pattern, shown in Fig. 3. During outbursts, the photon index increases as the countrate rises, and then saturates at the highest countrates. OJ 287 is never found in a flat-spectrum state when brightest. A correlation analysis for the whole data set gives a Spearman rank order correlation coefficient $r_s = 0.61$ and a Student’s T-test of $T_S = 23$. For $N=681$ observations, this corresponds to a probability of a random result of $P < 10^{-8}$. For the epoch including the 2016/17 outburst (blue data points of Fig. 3) we find $r_s = 0.55$, $T_S = 7.4$, and $P < 10^{-8}$ ($N=125$), and for the 2020 outburst (red data points) we obtain $r_s = 0.8$, $T_S = 11.8$, and $P < 10^{-8}$ ($N=79$). This analysis shows that the data are correlated. Always, the probability of a random result is $P < 10^{-8}$.

2.2 Swift UVOT

We also observed OJ 287 with the UV-optical telescope (UVOT; Roming et al. 2005) in all six filters [V (5468Å), B(4392Å),

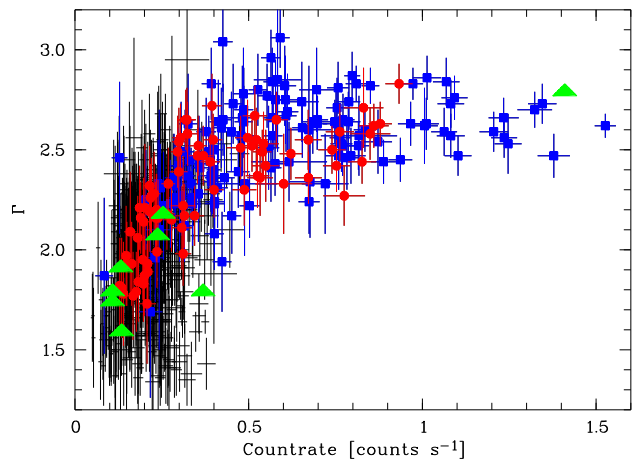


Figure 3. Variability of the photon index Γ_x of OJ 287 vs. Swift XRT countrate. A softer-when-brighter pattern is apparent (Sect. 2.1), confirming results of paper I. The time intervals including the two super-outbursts of OJ 287, in 2016–2017 and in 2020, are overplotted in blue (MJD 57673 – 58000) and red (MJD 58800 – 59100), respectively. Observations between 2005 and end of November 2020 are included in this plot. The eight XMM-Newton data sets were added for comparison (green triangles).

U(3465Å), UVW1(2600Å), UVM2(2246Å), UVW2(1928Å); where values in brackets are the filter central wavelengths] since the end of 2015 to obtain spectral energy distribution information of this rapidly varying blazar. Public archival data since 2005 were added to the analysis.

In each UVOT filter the observations were co-added. Source counts in all six filters were then selected in a circle of radius $5''$ while the background was determined in a nearby region of radius $20''$. The background-corrected counts were converted into fluxes based on the latest calibration as described in Poole et al. (2008) and Breeveld et al. (2010). In particular, the latest CALDB update version 20200925 which affects data since 2017 was employed.¹ The UVOT data were corrected for Galactic reddening with $E_{(B-V)}=0.0248$ (Schlegel et al. 1998), using a correction factor in each filter according to Equ. (2) of Roming et al. (2009) and based on the reddening curves of Cardelli et al. (1989).

3 XMM-NEWTON DATA ANALYSIS AND SPECTRAL FITS

3.1 Data preparation

We have analyzed all XMM-Newton (Jansen et al. 2001) observations of OJ 287 (Tab. 2). This includes our PI data from 2018–2020 (PI: S. Komossa/N. Schartel) and from 2005–2011 (PI: S. Ciprini) and an observation from 2015 (PI: R. Edelson).

While some XMM-Newton observations have been published before (e.g., Ciprini et al. 2007; Valtonen et al. 2012; Gaur et al. 2018; Gallant et al. 2018; Pal et al. 2020; Komossa et al. 2020a), here, we carry out a systematic analysis and comparison of all data sets in the context of the same model prescriptions and using the latest calibration data, and with some focus on our 2018 observation of April 18. That observation was carried out quasi-simultaneous

¹ <https://www.swift.ac.uk/analysis/uvot/index.php>

Table 2. Summary of XMM-Newton X-ray observations of OJ 287, where OBS-ID is the observation identification number, Δt_{total} is the observation duration in ks, and Δt_{eff} is the effective exposure time after epochs of flaring particle background were removed.

observation mode	OBS-ID	date	MJD	Δt_{total} (ks)	Δt_{eff} (ks)	comment
large-window	0300480201	2005-04-12	53472	18.5	4.6	hardest state, low flux level
large-window	0300480301	2005-11-03	53677	39.0	23	
large-window	0401060201	2006-11-17	54056	45.0	42	
large-window	0502630201	2008-04-22	54578	53.6	36	
large-window	0679380701	2011-10-15	55849	21.7	20	brightest state at $E > 5$ keV
large-window	0761500201	2015-05-07	57149	121.4	60	
large-window	0830190501	2018-04-18	58226	22.3	10.5	quasi-simultaneous with EHT observation
small-window	0854591201	2020-04-24	58963	13.3	9	super-soft state; highest flux level, taken at peak of 2020 outburst

with the EHT observation of OJ 287 on 2018 April 26–27 and with the GMVA+ALMA observation on 2018 April 15.

The observations span a wide range in spectral and flux states (Fig. 4). The majority of them was carried out in large-window mode when OJ 287 was at low-intermediate brightness states. The 2020 high-state observation was acquired in small-window mode. In these partial-window modes, only a part of the whole CCD is used to collect data in order to minimize the effect of photon pile-up.

The XMM-Newton data were reduced using the Science Analysis Software (SAS) version 18.0.0. Data were checked for epochs of flaring particle background, and the corresponding time intervals were excluded from the analysis resulting in effective exposure times listed in Tab. 2. EPIC-pn and EPIC-MOS spectra (Strüder et al. 2001) were extracted in a circular region of $20''$ radius centered on the source position, while background photons were collected in a nearby region of $\sim 50''$ for the pn and $\sim 100''$ for the MOS instruments. Reflection Grating Spectrometer (RGS; den Herder et al. 2001) data of the 2018 observation were inspected. We used RGSPROC with standard settings to extract the spectra and background for each detector, and combined the first order spectra from the two instruments into a single higher-signal spectrum. The pn and MOS data were binned to a signal-to-noise ratio of at least 6, and to oversample the instrumental resolution by a factor of at least 3. The RGS spectrum was rebinned by a factor of 8.

3.2 Spectral fits

To carry out the spectral analysis, spectra were fit with several emission models (Tab. 3) which are typical for the X-ray spectra of blazars, including a power law, a power law plus soft excess emission parametrized either as a black body component or second power law or a curved logarithmic parabolic power law model (logpar hereafter). These latter models are power laws with an index which varies as a log parabola in energy (Massaro et al. 2004), with $N(E) = N_0 (E/E_1)^{-(\alpha+\beta \log(E/E_1))}$, where N is the number of photons, N_0 is the normalization, E_1 is the pivot energy fixed at 1 keV, β is the curvature parameter, and α is the slope at the pivot energy. The various models are chosen with different scenarios in mind: the single power law is the most common emission model and visualizes the deviations from such a simple model, if any. In two-component models, a power law is always included to represent the high-energy emission component of OJ 287 typically of inverse Compton origin. A black body emission component is added to represent any kind of soft excess, including possibly (but unlikely) from any temporary accretion disk of the secondary SMBH. The logpar model is representative of a sum of different synchrotron components and is commonly used in the analysis of blazar spectra. Neutral absorption along our line-of-sight within our Galaxy is

always included (modeled with TBnew²; Wilms et al. 2000). In single-component power-law fits, additional absorption at $z = 0.306$ was added and left free to vary.³ χ^2 statistics were used to evaluate the goodness of the fit when carrying out the X-ray spectral analysis.

3.3 Spectral fit results

Results from single power-law fits of all data sets are displayed in Fig. 5. It is common to display fit residuals of single power-law fits, because these allow to visualize the residuals of this simple standard model, and facilitate comparison of past and future data of OJ 287 and also of other blazar X-ray spectra in a homogeneous way, using the same type of model description. Based on Fig. 5 we proceed with the discussion of X-ray spectral fit results.

As can be seen from Fig. 5, two XMM-Newton low-state spectra, taken in 2005a and 2008, are fit well by a single power-law component. Additional components are not required by the fit and are therefore largely unconstrained in a free fit. We return to these low-state spectra below, then taking into account what we have learned from fitting the other spectra.

The remaining spectra are not well fit by a single power law. The fit quality is not significantly improved when allowing for additional absorption intrinsic to OJ 287, which always turns out to be consistent with zero. The spectra require the presence of a second spectral component in addition to a single power law. Adding a second power law component or a logarithmic parabolic model fits the spectra well (Tab. 3 and Fig. 6), and with the exception of the 2020 data set when OJ 287 was brightest, the two models cannot be distinguished in terms of fit quality. The higher-energy component of the two-component power-law fit is always consistent with a photon index of $\Gamma_X = 1.5$ within the errors. Γ_X was therefore fixed to that value in the logpar plus power-law models.

The steeper power law with photon index in the range $\Gamma_X \approx 2 - 2.8$ (or the logarithmic parabolic model) accounts for the soft (low-energy) emission component which breaks into a harder power law component with $\Gamma_X \approx 1.5$ (in the two-component power-law models) up to 10 keV. A notable exception is the 2020 outburst

² <https://pulsar.sternwarte.uni-erlangen.de/wilms/research/tbabs/>

³ The most common source of absorption in blazars is the interstellar medium of the host galaxy. In rare cases, single BLR (or NLR) clouds of large column density can be located along the line of sight between the jet(knot) and the observer. Other sources of absorption (ionized or neutral) can be accretion-disk winds or ionized outflows driven by jet-cloud interactions.

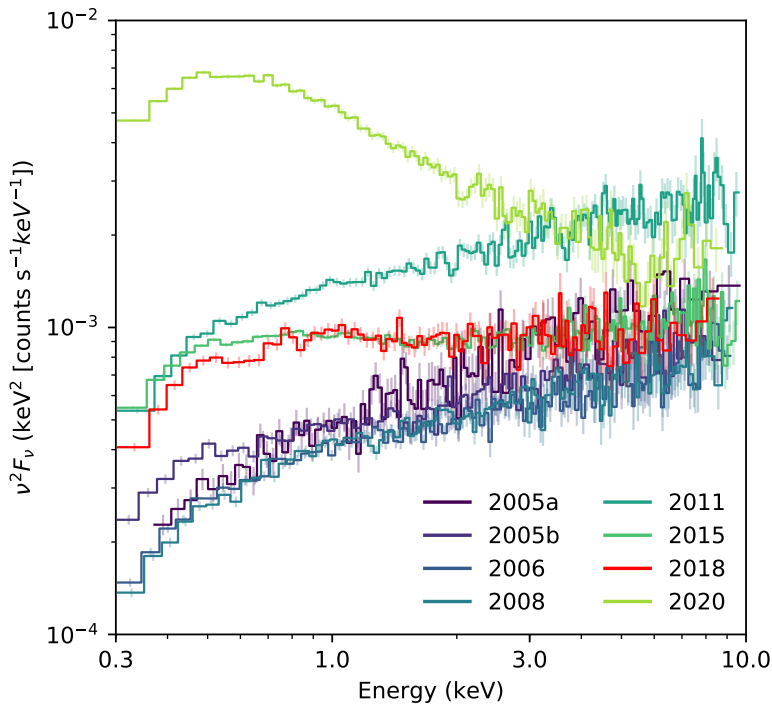


Figure 4. Comparison of all XMM-Newton EPIC-pn spectra of OJ 287 in the observer’s frame between 2005 and 2020, corrected for the effective area of the detector and uncorrected for Galactic absorption. Our 2018 data are highlighted in red, while other observations are marked with different colors and labelled by year of observation. Two spectral states are apparent. A "hard state" dominated by flat power-law emission, and a "soft state" with an additional low-energy component which becomes increasingly dominant when OJ 287 is X-ray bright. The super-soft emission component strongly dominates the 2020 outburst spectrum.

spectrum which requires a *significantly steeper hard X-ray component*. Fit results of the 2020 data were reported in paper I, and are provided in Tab. 3 for comparison.

The phenomenological black body representation of the soft emission component does not provide a successful fit to most of the spectra, including the highest-quality 2020 outburst spectrum which had the strongest soft excess, and we therefore do not discuss it any further, but keep it in Tab. 3 for comparison purposes.

Flux changes of OJ 287 are not only driven by the strength of the soft emission component; the hard X-ray emission is variable, too, albeit generally with lower amplitude. The 2011 XMM-Newton spectrum of OJ 287 stands out as showing the brightest flux above ~ 5 keV.

The break energy, where the soft and hard spectral components intersect, is located around 2 keV. It shifts to < 1 keV in the 2005b and 2006 low-state spectra, and to 4 keV in the 2020 outburst spectrum (Fig. 6).

Finally, we return to the low-state spectra of 2005a and 2008, which could be fit with single power laws. Since the two-component power-law fits of the other data sets always require a higher-energy spectral component with $\Gamma_x \approx 1.5$ and a lower-energy soft component, it is plausible to assume that the same holds for the 2005a and 2008 data, where the low photon statistics prevented a two-component spectral decomposition. As an example, we analyzed the 2008 data further, where $\Gamma_x = 1.75$. For a quantitative evaluation of the remaining contribution of a low-energy soft emission component to this spectrum, we have enforced a two-component fit with $\Gamma_{X,2}=1.5$. Then, $\Gamma_{X,1} \leq 2$, and up to 50% of the flux can be contained in such a soft component.

3.4 The 2018 data quasi-simultaneous with EHT

The 2018 observation, quasi-simultaneous with EHT, shows OJ 287 in an intermediate flux state. The spectrum shows two components. A hard power-law component with $\Gamma_x=1.5$, and a second soft emission component with $\Gamma_x=2$. Given possible hints of spectral complexity below ~ 1 keV (Figs 5, 7), the 2018 data were carefully compared with the 2015 exposure where OJ 287 was in a similar flux state. Further, the pn and MOS spectra of the 2018 observation were inspected and compared, revealing that fine structures around 0.8 keV in the pn data are not present in MOS and are therefore not statistically significant (Fig. 7). Independently, RGS data were inspected for the presence of strong narrow emission or absorption features. None were individually identified (Fig. 8). When an ionized absorber component is added to the spectral fit using the `xabs` model (Steenbrugge et al. 2003) the quality of the spectral fit is not significantly improved. Most likely, the small deficit of photons below 1 keV in 2018 as compared to 2015 is due to a slightly fainter soft emission component in 2018.

3.5 Short timescale variability

The longest observation of OJ 287 was carried out in 2015 with a duration of 121 ks. Since OJ 287 is highly variable on timescales of days and longer, this light curve was inspected for shorter timescale variability and flaring. Since $\sim 50\%$ of the observation was affected by episodes of background flaring which dominate the emission at > 2 keV, only the full (0.3–1.5) keV light curve was analyzed. Some limited variability is visible on relatively long timescales (10s of ks), with no clear evidence for rapid variability. We calculate

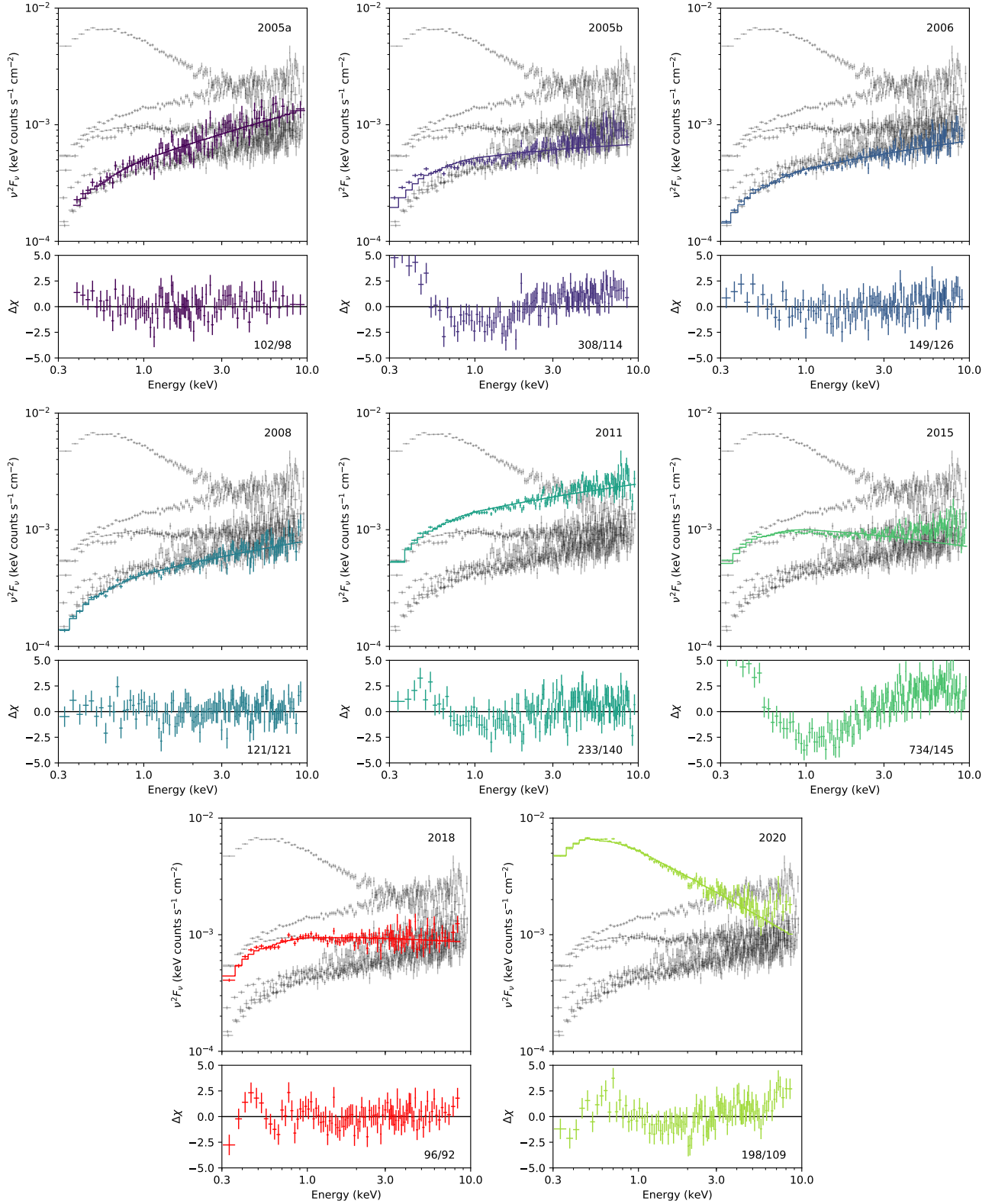


Figure 5. Mosaic of single power-law model fits of the XMM-Newton data of OJ 287 and fit residuals in the observer's frame. Each sub-plot corresponds to one XMM-Newton observation of OJ 287 as marked in the upper right corner. The fit statistics are reported in the lower right corner. The residuals are plotted in units of standard deviations, so that structure at low energies is visible and the residuals are not dominated by noisy low-signal bins at high energies.

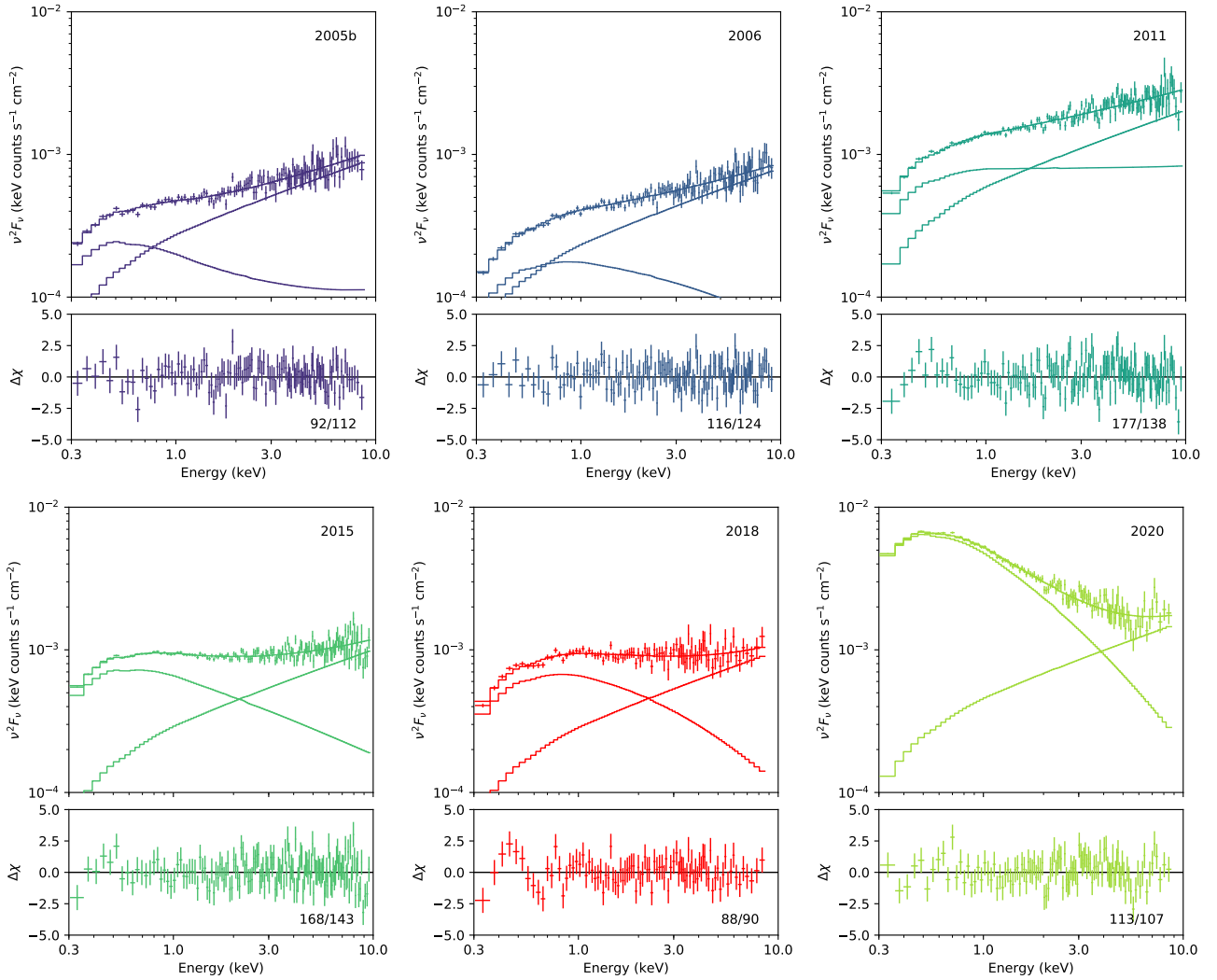


Figure 6. Best-fit logpar plus power law models of those XMM-Newton observations of OJ 287 that require a second component beyond a single power law. Each sub-plot corresponds to one XMM-Newton observation of OJ 287. The date is marked in the upper right corner and the fit statistics in the lower right corner. The soft (low-energy) emission component is always the logpar model, while the hard (high-energy) emission component is always the power law.

the fractional root mean square (RMS) variability amplitude F_{var} (e.g. Vaughan et al. 2003) for this light curve, finding a small but significant (dimensionless) value of $F_{\text{var},s} = 0.033 \pm 0.002$. Since the hard X-ray band is affected by multiple episodes of background flaring (Sect. 3.1), we only analyzed the first good contiguous 40 ks of the hard-band light curve and find $F_{\text{var},h} = 0.04 \pm 0.01$.

4 DISCUSSION

The spectral energy distribution (SED) of blazars shows two emission maxima (for reviews see: Marscher 2009; Ghisellini 2015). One at low energies peaking between the sub-mm and EUV, sometimes extending into the X-ray regime, and explained as synchrotron radiation of the jet electrons. And a second maximum in the hard X-ray/ γ -ray regime, usually explained as inverse Compton (IC) radiation from photons located either within the jet (synchrotron-self-Compton process; SSC) or from external seed photons emitted by the broad-line region or torus (external Comptonization; EC). Other radiation mechanisms might contribute as well. In hadronic models

the high-energy emission is dominated by ultra-relativistic protons (Böttcher 2019). The SED-type of OJ 287 was classified as LSP (low synchrotron peak frequency; $< 10^{14}$ Hz; Abdo et al. (2010)) or ISP (intermediate synchrotron peak frequency; between 10^{14} and 10^{15} Hz; Ackermann et al. (2011)). An additional thermal component in its broad-band SED was identified at epochs close to the impact flare predicted by the SMBBH model (Ciprini et al. 2007; Ciprini 2018; Valtonen et al. 2012).

Previous observations suggested that variability in X-rays of OJ 287 is driven primarily by a mix of the SSC component and synchrotron emission. However, most previous missions did not allow multi-component spectral fits, and during the 2020 XMM-NuSTAR high-state (paper I), the high-energy power-law component was steeper than expected for pure IC emission models which produce hard spectra with $\Gamma_X \approx 1.5$ (Kubo et al. 1998; Isobe et al. 2001). We discuss implications from the XMM-Newton spectral fits below.

Table 3. Spectral fit results of all XMM-Newton observations of OJ 287. Fits to the 2020 data were already reported in paper I. Representative models are repeated here for comparison with the earlier observations. Neutral absorption of the Galactic value $N_{\text{H,Gal}}$ is included in all fits. Parameters and abbreviations are as follows: (1) Models: pl = power law, bbdy = black body, logpar = logarithmic parabolic model; (2) absorption column density in units of 10^{20} cm^{-2} ; (3) power-law photon index; (4) unabsorbed power-law flux (f_1 , f_2) or logpar flux (f_{lp}) from (0.5–10) keV in units of $10^{-12} \text{ erg s}^{-1} \text{ cm}^{-2}$ (rest frame); (5) black body temperature kT_{BB} in units of keV; (6) (0.5–10) keV black body flux in units of $10^{-12} \text{ erg s}^{-1} \text{ cm}^{-2}$ (rest frame); (7) curvature parameter β and (8) spectral index α of the logpar model; (9) goodness of fit χ^2 and number of degrees of freedom. When no errors are reported, the quantity was fixed. The spectral fits of the NuSTAR data, taken from paper I, are shown for comparison. For NuSTAR data, the pl flux is given from 3–50 keV.

model (1)	N_{H} (2)	$\Gamma_{1,\text{soft}}$ (3)	f_1 (4)	$\Gamma_{2,\text{hard}}$ (3)	f_2 (4)	kT_{BB} (5)	f_{BB} (6)	β (7)	α (8)	f_{lp} (4)	χ^2/n_{dof} (9)
2020, highest state											
pl	2.49	2.82 ± 0.01	38.5 ± 0.1	-	-	-	-	-	-	-	476/284
bbdy + pl	2.49	2.70 ± 0.01	35.2 ± 0.3	-	-	0.152 ± 0.003	3.2 ± 0.4	-	-	-	343/282
logpar + pl	2.49	-	-	2.2	17.3 ± 0.6	-	-	0.8 ± 0.1	3.22 ± 0.03	21.5 ± 0.6^1	286/282
pl (NuSTAR)	2.49	-	-	2.36 ± 0.06	6.1 ± 0.2	-	-	-	-	-	74/74
pl (NuSTAR, >10 keV)	2.49	-	-	2.2 ± 0.2	-	-	-	-	-	-	-
2018, simultaneous with EHT											
pl	2.49	2.08 ± 0.01	8.10 ± 0.07	-	-	-	-	-	-	-	96/92
pl, N_{H} free	< 0.7 + 2.49	$2.08^{+0.03}_{-0.02}$	8.1 ± 0.1	-	-	-	-	-	-	-	96/91
bbdy + pl	2.49	2.02 ± 0.03	7.8 ± 0.1	-	-	0.20 ± 0.02	0.3 ± 0.1	-	-	-	89/90
pl + pl	2.49	$2.12^{+0.02}_{-0.01}$	7.2 ± 0.6	< 1.55	0.9 ± 0.6	-	-	-	-	-	93/90
logpar + pl	2.49	-	-	1.5	$3.7^{+0.4}_{-0.6}$	-	-	0.41 ± 0.16	2.30 ± 0.05	$4.5^{+0.6}_{-0.4}$	87/90
2015											
pl	2.49	2.188 ± 0.005	8.25 ± 0.03	-	-	-	-	-	-	-	734/145
pl, N_{H} free	< 0.01 + 2.49	2.19 ± 0.01	8.25 ± 0.08	-	-	-	-	-	-	-	734/144
bbdy + pl	2.49	2.00 ± 0.01	7.91 ± 0.04	-	-	0.130 ± 0.003	0.69 ± 0.04	-	-	-	222/143
pl + pl	2.49	$2.41^{+0.02}_{-0.01}$	$4.7^{+0.3}_{-0.5}$	1.54 ± 0.08	$3.9^{+0.6}_{-0.3}$	-	-	-	-	-	168/143
logpar + pl	2.49	-	-	1.5	$3.7^{+0.3}_{-0.4}$	-	-	0.013 ± 0.008	$2.58^{+0.03}_{-0.04}$	$4.90^{+0.4}_{-0.3}$	167/143
2011											
pl	2.49	1.799 ± 0.006	14.39 ± 0.08	-	-	-	-	-	-	-	233/140
bbdy + pl	2.49	1.72 ± 0.01	14.2 ± 0.1	-	-	0.15 ± 0.01	0.46 ± 0.07	-	-	-	166/138
pl + pl	2.49	2.4 ± 0.3	$2.9^{+2.9}_{-1.6}$	1.6 ± 0.1	$11.7^{+1.6}_{-2.9}$	-	-	-	-	-	177/138
logpar + pl	2.49	-	-	1.5	$7.5^{+2.2}_{-5.6}$	-	-	$7.1^{+5.6}_{-2.2}$	1.6 ± 0.1	$4.1^{+3.8}_{-1.4}$	177/138
2008											
pl	2.49	1.752 ± 0.009	4.34 ± 0.03	-	-	-	-	-	-	-	121/121
pl + pl	2.49	< 2	2.0 ± 0.1	1.5	2.3 ± 0.1	-	-	-	-	-	121/120
2006											
pl	2.49	1.80 ± 0.01	4.23 ± 0.03	-	-	-	-	-	-	-	149/126
bbdy + pl	2.49	1.74 ± 0.02	4.19 ± 0.04	-	-	0.14 ± 0.02	0.10 ± 0.02	-	-	-	123/124
pl + pl	2.49	$1.96^{+0.29}_{-0.05}$	$1.7^{+0.2}_{-0.9}$	< 1.6	$2.6^{+0.8}_{-0.2}$	-	-	-	-	-	116/124
logpar + pl	2.49	-	-	1.5	< 5.5	-	-	$0.17^{+0.24}_{-0.37}$	$2.2^{+0.1}_{-0.3}$	$1.3^{+4.2}_{-0.2}$	116/124
2005-11 (2005b)											
pl	2.49	1.92 ± 0.01	4.85 ± 0.04	-	-	-	-	-	-	-	308/114
bbdy + pl	2.49	1.75 ± 0.02	4.83 ± 0.05	-	-	0.106 ± 0.007	0.31 ± 0.03	-	-	-	99/112
pl + pl	2.49	> 2.95	$1.12^{+0.08}_{-0.06}$	1.54 ± 0.03	4.04 ± 0.07	-	-	-	-	-	92/112
logpar + pl	2.49	-	-	1.5	$3.5^{+0.3}_{-0.5}$	-	-	$-0.4^{+0.2}_{-0.1}$	2.7 ± 0.1	$1.6^{+0.5}_{-0.3}$	92/112
2005-04 (2005a)											
pl	2.49	1.60 ± 0.02	5.9 ± 0.1	-	-	-	-	-	-	-	102/98

¹ Note: in paper I (Tab. 2), the flux entry for the logpar component of this model was a typo, now corrected.

4.1 Softer-when-brighter variability pattern

OJ 287 exhibits a softer-when-brighter variability pattern in our multi-year Swift light curve (Fig. 3; see also Komossa et al. 2017), previously sporadically seen on long timescales when combining a few Einstein, EXOSAT, ROSAT, and ASCA data (Isobe et al. 2001; Urry et al. 1996), but absent at another epoch (Seta et al. 2009; Szejkowski & Wiercholska 2017).

The Swift XRT light curve, containing 681 data points obtained with the same instrument, for the first time puts the softness-brightness behaviour on a firm statistical basis and also traces short timescales of days, weeks, and months, and reveals details of the

correlation. While the short snapshot observations with Swift do not contain enough photons to permit multi-component spectral decompositions, the much deeper observations with the more sensitive detectors aboard XMM-Newton allowed us to decompose the spectra into multiple components spanning 15 years of observations. These components will be discussed in the next sections. In particular, the spectral analysis of the XMM-Newton observation of 2011 has shown that variability of the high-energy spectral component (Fig. 4) contributes to the scatter in the softer-when-brighter variability at low countrates ($< 0.5 \text{ cts s}^{-1}$). This epoch of observation coincides with γ -ray flaring activity of OJ 287 (e.g., Escande &

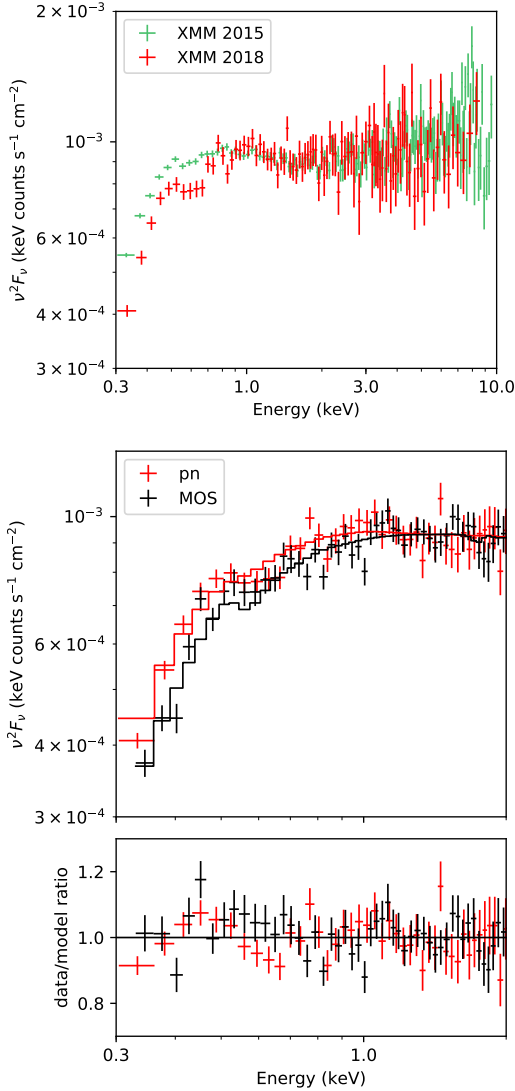


Figure 7. 2018 XMM-Newton EPIC pn and EPIC MOS spectra of OJ 287 it was at intermediate flux level, observed quasi-simultaneous with EHT. The upper panel shows a comparison between the 2015 and 2018 EPIC pn data, where OJ 287 was overall in a similar state but shows a small low-energy deficiency in flux in 2018. The lower panels compare the EPIC pn and EPIC MOS data of 2018.

Schinzel 2011; Hodgson et al. 2017; Goyal et al 2018) of which we see the low-energy tail in the XMM-Newton band.

4.2 Synchrotron component(s) at high-state

Which mechanism drives the super-soft component of the X-ray spectrum in high-states: accretion or jet (synchrotron) activity? We can safely establish that the 2020 outburst is powered by jet emission, because (1) the rapid X-ray variability is inconsistent with the large SMBH mass of the primary (faster than the light crossing time at the last stable orbit of the accretion disk; paper I), (2) the accompanying radio flare in 2020 (Komossa et al. 2020c) implies jet emission in the radio regime, (3) the high optical polarization (Zola et al. 2020) implies jet emission in the optical, too, and (4) the correlated (radio)-optical-UV-X-ray emission then implies jet emission in all bands.

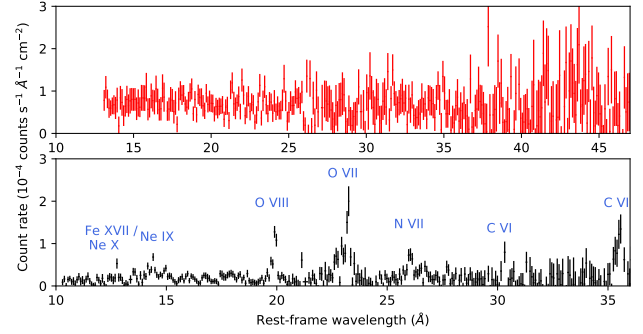


Figure 8. 2018 RGS spectrum of OJ 287 (upper panel) in comparison with the RGS spectrum of a Seyfert galaxy (lower panel; both spectra in observer frame) which exhibits strong emission lines from common elements and transitions, labelled in blue (Mrk 335; Parker et al. 2019). No narrow features are detected in the RGS spectrum of OJ 287.

The second large X-ray outburst of OJ 287 was in late 2016 – early 2017 (our Fig. 1; Komossa et al. 2017), and given its similarities with the 2020 outburst and additional arguments, we argue that it was jet-powered, too. It shows the very same softer-when-brighter variability pattern (established in our Fig. 3), it was accompanied by a radio outburst (Myserlis et al. 2018; Lee et al. 2020) and by VHE emission (O’Brien 2017), and the radio polarization was very high during a contemporaneous ALMA observation (Goddì et al. 2021).

Interestingly, during the 2020 outburst, where we obtained a dedicated XMM-Newton and NuSTAR observation at the peak of the outburst, the X-ray spectrum is more complicated than a superposition of a low-energy synchrotron and high-energy IC component. Besides the very soft emission component well described by a logpar model, the power-law component which extends well above 10 keV is steeper than expected from IC emission alone and we therefore consider it to be a third spectral component. It may plausibly indicate a mix of a flat IC component with a second independent synchrotron component extending well above 10 keV only appearing at outburst, or alternatively could represent temporary enhanced emission from an accretion disk corona. While we resolve the emitting components spectroscopically, high-resolution radio observations hold the promise to locate the synchrotron emission components spatially. No EHT observations were carried out in 2020, but they are expected to continue in upcoming years. The unusual second 2020 (synchrotron or coronal) high-state component adds to making OJ 287 an interesting target in upcoming EHT campaigns.

The rapid variability of the multiple synchrotron components is reminiscent of the erratic jet model of Agudo et al. (2012), who involve multiple injections from a turbulent and/or clumpy disk to explain (short-term) erratic wobbling of the inner jet observed in VLBA data of OJ 287 on the order of months. The frequent secondary impacts on the accretion disk around the primary predicted by the binary SMBH model of OJ 287 might contribute to enhancing inhomogeneities/turbulence in the accretion disk of OJ 287. Additionally, Valtonen & Pihajoki (2013) and Dey et al. (2021) explain the long-term systematic trends in the wobble by variations in the initial jet launching angle in the binary system.

4.3 Low-state emission

During X-ray low-states of OJ 287, the soft (synchrotron) component is much fainter or entirely absent, and the XMM-Newton X-ray spectrum is well fit by a flat power-law component as flat as $\Gamma_x \approx 1.5$, indicating IC emission (in the framework of leptonic jet models). Similarly, the flattest X-ray states of OJ 287 detected with Swift are well described by a single power law with photon index 1.5.

We use the 2008 low-state of OJ 287 measured with XMM-Newton to estimate the low-state *isotropic* X-ray luminosity, and take it as a strict *upper limit* on any long-lived accretion disk contribution to the X-ray spectrum of OJ 287. With $L_{x,iso} = 1.3 \times 10^{45}$ erg s⁻¹ this gives $L_x/L_{Edd} \leq 5.6 \times 10^{-4}$ ($M_{BH,primary} = 1.8 \times 10^{10} M_\odot$) or $L_x/L_{Edd} \leq 6.7 \times 10^{-2}$ ($M_{BH,secondary} = 1.5 \times 10^8 M_\odot$) for any accretion disk contribution in X-rays.

4.4 Binary black hole model

In the context of the SMBBH model of OJ 287 (recently reviewed by Dey et al. 2019), the main site of multi-wavelength emission is still the jet of the primary SMBH, but there are also episodes where the thermal bremsstrahlung emission from the secondary's impact on the accretion disk around the primary (Ivanov et al. 1998) dominates the spectrum in the IR to UV bands (e.g., Laine et al. 2020). In addition, there is delayed temporary enhanced accretion on the primary (triggering new jet activity), following the disk impact events. Even though the observed low-state X-rays of OJ 287 are dominated by jet activity and consistent with IC emission, we used the low-state X-ray flux to estimate an upper limit on any long-lived emission from the accretion disk in X-rays (Sect. 4.3). Assuming a factor-of-10 bolometric correction (Elvis et al. 1994), this then translates into a very low $L/L_{Edd} \leq 5.6 \times 10^{-3}$ for $M_{BH,primary} = 1.8 \times 10^{10} M_\odot$. However, this estimate is uncertain for several reasons. For instance, we do not know the disk emission efficiency η , and it is possible that OJ 287 accretes near Eddington, but the gas emissivity is low. Second, as the SMBH mass increases, we expect to see less (multi-temperature black body) emission from the actual accretion disk extending into the soft X-ray regime (Done et al. 2012), but still expect the presence of hard emission from the corona above the disk (and reprocessing signatures at soft X-rays). Bolometric corrections are therefore more uncertain at the highest SMBH masses. They also depend on accretion rate (Vasudevan & Fabian 2009; Grupe et al. 2010). The mass of the primary SMBH itself is very well constrained to be above $10^{10} M_\odot$ in the binary SMBH model (Pietilä 1998; Dey et al. 2018). Since previous modelling of OJ 287 in the context of the binary SMBH model requires an accretion rate of $\sim 10\%$ Eddington (Valtonen et al. 2019), within this model the X-ray observations then imply that the disk corona of OJ 287 is under-luminous in X-rays. It is not expected that the corona is completely absent, as the model assumes a highly magnetized accretion disk.

Swift recorded two major X-ray–optical outbursts of OJ 287 in 2016–17 and 2020 (Fig. 1). Both outbursts are driven by synchrotron emission. Based on predictions (Sundelius et al. 1997) of the SMBBH model of OJ 287, (Komossa et al. 2020a) concluded that the 2020 outburst is consistent with an after-flare which followed the 2019 impact flare of OJ 287. It is tempting to speculate that, similarly, the 2016–17 X-ray outburst was the after-flare of the 2015 impact flare. Alternatively, it could represent jet flaring activity unrelated to the binary. In the after-flare interpretation, the larger time delay then arises because the secondary's disk impact

site was further out in 2015 at larger distance from the primary (Dey et al. 2018; Valtonen et al. 2019). The after-flare interpretation was already suggested based on *optical* high-state observations and high levels of polarization lasting until the end of 2016 (Valtonen et al. 2017). The X-ray high-state continues into the first months of 2017 and reaches its maximum in early 2017.

With highest-resolution radio observations including EHT, we may be able to resolve the synchrotron outburst components in the radio regime, and locate the outburst emission within the nuclear region. Especially, if the new jet component is powered by a (binary-triggered) new jet event, it will be located in the core; if it is rather an unrelated jet-ISM shock, it could be significantly off-nuclear.

5 SUMMARY AND CONCLUSIONS

Based on 1.5 decades of XMM-Newton spectroscopy and Swift monitoring of OJ 287 (densely since 2015 in our dedicated MOMO program aimed at testing facets of the binary SMBH model and studying disk and jet physics of this nearby, bright blazar), the following conclusions are reached:

- OJ 287 displays a strong softer-when-brighter spectral variability pattern, clearly established on the basis of ~ 700 Swift observations.
- The spectral variability between 0.3–10 keV is extreme. It encompasses all spectral states observed in blazars in that band, from ultra-steep to very flat ($\Gamma_x = 2.8 - 1.5$).
- With XMM-Newton and NuSTAR, we distinguish between three different spectral components of OJ 287: (1) The first spectral state is a low/hard state with photon index $\Gamma_x \approx 1.5$, dominated by inverse-Compton emission. (2) The second spectral state is a high/soft state dominated by synchrotron emission well described by a logarithmic parabolic power-law model or with an equivalent single photon index as steep as $\Gamma_x \sim 2.8$ in outburst. The softer-when-brighter variability behaviour is explained by the systematic increase of the synchrotron component as OJ 287 brightens. (3) An additional spectral component is detected in outburst in 2020, with a relatively steep power law of index 2.2 ± 0.2 beyond 10 keV observed with NuSTAR and first identified in paper I, likely representing a mix of IC with a second independent synchrotron component.
- OJ 287 is highly variable, with rapid flaring on the timescale of days, faster than the light-crossing time near the last stable orbit (paper I). However, the fractional variability amplitude on shorter timescales during a 120 ks XMM-Newton long-look at intermediate flux levels, $F_{var} = 0.033 \pm 0.002$, is small.
- The 2018 XMM-Newton spectrum which was obtained quasi-simultaneous with EHT shows OJ 287 in a typical intermediate-flux state and is well described by a two-component model, involving a hard power law component with $\Gamma_x = 1.5$, and a second soft emission component in form of a logarithmic parabolic model or a single power law of photon index 2; interpreted as inverse-Compton and synchrotron emission, respectively.
- The Eddington ratio L_x/L_{Edd} of OJ 287 is surprisingly low in X-rays. The low-state emission constrains any long-lived accretion-disk/corona contribution to $L_x/L_{Edd} \leq 5.6 \times 10^{-4}$ for $M_{BH} = 1.8 \times 10^{10} M_\odot$, implying that the disk corona of OJ 287 is under-luminous in X-rays.
- We suggest that the 2016/17 X-ray outburst of OJ 287 is related to the 2016 optical outburst which was noted earlier and was interpreted as an after-flare predicted by the binary SMBH model. Highest-resolution radio observations have the potential to locate

the jet-emitting components within the nucleus and follow their evolution in the future.

- Our most recent Swift observations revealed a deep low-state in September 2020, followed by a gradual recovery in flux.

Given its brightness, proximity, and candidate binary SMBH nature, OJ 287 is a remarkable multi-messenger source that can be well studied already, well before the actual direct detection of gravitational waves from supermassive black hole systems.

ACKNOWLEDGEMENTS

We would like to thank the Swift and XMM-Newton teams for carrying out our observations and our anonymous referee for their useful comments and suggestions. JLG acknowledges financial support from the Spanish Ministerio de Economía y Competitividad (grants AYA2016-80889-P, PID2019-108995GB-C21), the Consejería de Economía, Conocimiento, Empresas y Universidad of the Junta de Andalucía (grant P18-FR-1769), the Consejo Superior de Investigaciones Científicas (grant 2019AEP112), and the State Agency for Research of the Spanish MCIU through the Center of Excellence Severo Ochoa award for the Instituto de Astrofísica de Andalucía (SEV-2017-0709). SGJ acknowledges financial support from NASA Fermi GI grants 80NSSC20K1565 and 80NSSC20K1566. DH acknowledges funding from the Natural Sciences and Engineering Research Council of Canada (NSERC) and the Canada Research Chairs (CRC) program. We acknowledge the use of data we have obtained with the Neil Gehrels Swift mission. We also acknowledge the use of public data from the Swift data archive. This work made use of data supplied by the UK Swift Science Data Centre at the University of Leicester. This research is partly based on observations obtained with XMM-Newton, an ESA science mission with instruments and contributions directly funded by ESA Member States and NASA. This research has made use of the XRT Data Analysis Software (XRTDAS) developed under the responsibility of the ASI Space Science Data Center (SSDC), Italy.

DATA AVAILABILITY STATEMENT

Reduced data are available upon reasonable request. Raw data can be retrieved from the Swift and XMM-Newton archives at <https://swift.gsfc.nasa.gov/archive/> and <https://www.cosmos.esa.int/web/xmm-newton>, respectively.

REFERENCES

- Abdo A.A., et al. 2010, *ApJ* 716, 30
 Ackermann M., et al. 2011, *ApJ* 743, 171
 Agudo I., et al. 2011, *ApJ* 735, L10
 Agudo I., et al. 2012, *ApJ* 747, 63
 Aller M.F., et al. 2014, *ApJ* 791, 53
 Arnaud K.A., 1996, *ASPC* 101, 17
 Begelman M.C., Blandford R.D., Rees M.J. 1980, *Nature* 287, 307
 Böttcher M., 2019, *Galaxies* 7, 20
 Breeveld A.A., et al. 2010, *MNRAS* 406, 1687
 Britzen S., et al. 2018, *MNRAS* 478, 3199
 Burrows D.N., et al. 2005, *SSRv* 120, 165
 Cardelli J.A., et al. 1989, *ApJ* 345, 245
 Centrella J., et al. 2010, *RevModPhys* 82, 3069
 Ciprini S., et al. 2007, *MmSAI* 78, 741
 Ciprini S., 2018, in *PoS APCS2018: Accretion Processes in Cosmic Sources - II*, 41
 Cohen M.H., et al. 2018, *ApJ* 862, 1
 Colpi M., 2014, *SSRv* 183, 189
 Comastri A., Molendi S., Ghisellini G., 1995, *MNRAS* 277, 297
 den Herder J.W., et al. 2001, *A&A* 365, L7
 Dey L., et al. 2018, *ApJ* 866, 11
 Dey L., et al. 2019, *Universe* 5, 108
 Dey L., et al. 2021, *MNRAS*, submitted
 Dickel J.R., et al. 1967, *AJ* 72, 757
 Done C., et al. 2012, *MNRAS* 420, 1848
 Elvis M., et al. 1994, *ApJS* 95, 1
 Escande L., Schinzel F.K., 2011, *Astron. Telegram* 3680, 1
 Evans, P., et al. 2007, *A&A*, 469, 379
 Event Horizon Telescope Collaboration, Akiyama K., et al. 2019, *ApJ* 875, L1
 Gallant D., Gallo L.C., Parker M.L., 2018, *MNRAS* 480, 1999
 Gaur H., et al. 2018, *MNRAS* 473, 3638
 Gehrels N., et al. 2004, *ApJ* 611, 1005
 Ghisellini G., 2015, *JHEAp* 7, 163
 Goddi C., et al. 2021, *ApJ* 910, L14
 Goyal A., et al. 2018, *ApJ* 863, 175
 Graham M.J., et al. 2015, *MNRAS* 453, 1562
 Grupe D., et al. 2010, *ApJS* 187, 64
 Grupe D., Komossa S., Gomez, J.L., 2016, *Astron. Telegram* 9629, 1
 Grupe D., Komossa S., Falcone A., 2017, *Astron. Telegram* 10043, 1
 Hill J.E., et al. 2004, *SPIE* 5165, 217
 Hodgson J.A., et al. 2017, *A&A* 597, A80
 Idesawa E., et al. 1997, *PASJ* 49, 631
 Isobe N., et al. 2001, *PASJ* 53, 79
 Ivanov P.B., Igmenshchev I.V., Novikov I.D., 1998, *ApJ* 507, 131
 Jansen F., et al. 2001, *A&A* 365, L1
 Jorstad S.G., et al. 2005, *AJ* 130, 1418
 Kalberla P.M.W., et al. 2005, *A&A* 440, 775
 Katz J.I., 1997, *ApJ* 478, 527
 Kelley L., et al. 2019, *BAAS* 51, 490
 Komossa S., et al. 2015, *Astron. Telegram* 8411, 1
 Komossa S., Zensus J.A., 2016, *IAUS* 312, 13
 Komossa S., et al. 2017, *IAUS* 324, 168
 Komossa S., Grupe D., Gómez J.L., 2018, *Astron. Telegram* 12086, 1
 Komossa S., et al. 2020a, *MNRAS* 498, L35 (paper I)
 Komossa S., Grupe D., Gómez J.L., 2020b, *Astron. Telegram* 13658, 1
 Komossa S., et al. 2020c, *Astron. Telegram* 13702, 1
 Komossa S., et al. 2020d, *Astron. Telegram* 14052, 1
 Kraus J.D., 1977, *Vistas in Astronomy* 20, 445
 Kubo H., et al. 1998, *ApJ* 504, 693
 Kushwaha P., et al. 2018, *MNRAS* 473, 1145
 Laine S., et al. 2020, *ApJL* 894, L1
 Lee J.W., et al. 2020, *ApJ* 902, 104
 Lehto H.J., Valtonen M.J., 1996, *ApJ* 460, 207
 Liu F.K., Wu X.B., 2002, *A&A*, 388, L48
 Madejski G.M., Schwartz, D.A., 1988, *ApJ* 330, 776
 Marscher A.P., 2009, *Lect. Notes Phys.* 794; arXiv:0909.2576
 Marscher A.P., Jorstad S.G., 2011, *ApJ* 729, 26
 Massaro E., et al. 2003, *A&A* 399, 33
 Massaro E., et al. 2004, *A&A* 413, 489
 Massaro E., et al. 2008, *A&A* 489, 1047
 Mukherjee R., VERITAS Collaboration, 2017, *Astron. Telegram* 10051, 1
 Myserlis I., et al. 2018, *A&A* 619, 88
 Nilsson K., et al. 2010, *A&A* 516, A60
 O'Brien S., 2017, in *Proceedings of the 35th International Cosmic Ray Conference (ICRC 2017)*, arXiv:1708.02160
 Pal M., et al. 2020, *ApJ* 890, 47
 Parker M.L., et al. 2019, *MNRAS* 490, 683
 Pietilä H., 1998, *ApJ* 508, 669
 Pihajoki P., et al. 2013, *ApJ* 764, 5
 Poole T.S., et al. 2008, *MNRAS* 391, 1163
 Qian S.J., 2015, *RAA* 15, 687
 Roming P.W.A., et al. 2005, *SSRv* 120, 95
 Roming P.W.A., et al. 2009, *ApJ* 690, 163

- Sambruna R.M., et al. 1994, ApJ 434, 468
Schlegel D.J., Finkbeiner D.P., Davis M., 1998, ApJ 500, 525
Seta H., et al. 2009, PASJ 61, 1011
Siejkowski H., Wiercholska A., 2017, MNRAS 468, 426
Sillanpää A., et al. 1988, ApJ 325, 628
Sitko M.L., Junkkarinen V.T., 1985, PASP 97, 1158
Steenbrugge K.C., Kaastra J.S., de Vries C.P., Edelson R., 2003, A&A 402, 477
Stickel M., Fried J.W., Kuehr H., 1989, A&AS 80, 103
Stroh M.C., Falcone A.D., 2013, ApJS 20, 28
Strüder L., et al. 2001, A&A 365, L18
Sundelius B., et al. 1997, ApJ 484, 180
Urry, M., et al., 1996, ApJ 463, 424
Valtaoja E., et al. 2000, ApJ 531, 744
Valtonen M.J., et al. 2008, Nature 452, 851
Valtonen M.J., et al. 2009, ApJ 698, 781
Valtonen M.J., Ciprini S., Lehto H.J., 2012, MNRAS 427, 77
Valtonen M.J., Pihajoki P., 2013, A&A 557, A28
Valtonen M.J., et al. 2016, ApJL 819, L37
Valtonen M.J., et al. 2017, Galaxies 5, 83
Valtonen M.J., et al. 2019, ApJ 882, 88
Vasudevan R.V., Fabian A.C., 2009, MNRAS 392, 1124
Vaughan S., et al., 2003, MNRAS, 345, 1271
Villata M., et al. 1998, MNRAS 293, L13
Williamson K.E., et al. 2014, ApJ 789, 135
Wilms J., Allen A., McCray R., 2000, ApJ 542, 914
Wright E.L., 2006, PASP 118, 1711
Yardley, D.R.B., et al. 2010, MNRAS 407, 669
Zola S., et al. 2020, Astron. Telegram 13637, 1

This paper has been typeset from a \TeX/L\AA\TeX file prepared by the author.